Environmental (S)TEM Studies of Gas–Liquid–Solid Interactions under Reaction Conditions

Pratibha L. Gai, Renu Sharma, and Frances M. Ross

Abstract

We review the development of time-resolved, high-resolution environmental scanning/transmission electron microscopy [E(S)TEM] for directly probing dynamic gas–solid, liquid–solid, and gas–liquid–solid interactions at the atomic level. Unlike a regular TEM, such a microscope allows us to use high gas pressures (up to 40 mbars) in the sample region. The unique information available from experiments performed using E(S)TEM has enabled visualization of the dynamic nature of nanostructures during reactions. Such information can be directly applied to the development of advanced nanomaterials such as carbon nanotubes, silicon nanowires and processes, including the design of novel routes to polymers synthesis, and has aided in the identification of important phenomena during catalysis, chemical vapor deposition, and electrochemical deposition.

Introduction

The synthesis and functioning of technologically important materials, including catalysts, is often a direct result of their interactions with gases or liquids at elevated temperature. Deeper insights into dynamic surface phenomena and nanostructures at the nanoscale not only help us to understand structure–property relationships under reaction conditions, but also assist us in selectively synthesizing nanostructured materials with a desired structure or properties. Traditional investigations related to nanostructured materials have relied upon observations made before and after a reaction. However, to obtain insights into active sites and the operation mode, it is important to observe nanomaterials *in situ,* under reaction conditions. *In situ* environmental scanning/ transmission electron microscopy [E(S)TEM and ETEM] provides us with the possibility of directly probing dynamic processes in real time.

Catalytic materials have been traditionally used in many chemical processes but recently are also being employed for the synthesis of nanostructured materials such as nanotubes and nanowires. Catalysts generally lower the energy barrier of a chemical process. However, their activity is often reduced over a period of use because of changes in surface area (coalescence) or reaction with contaminants or reaction products (poisoning). Therefore, it is important to understand the nanoscale chemical and structural changes occurring in the catalyst (bulk as well as surface) under reaction conditions to optimize and maintain the catalytic properties. Techniques such as extended x-ray absorption fine structure, x-ray photoemission spectroscopy, Raman, x-ray diffraction, and scanning tunneling microscopy can be employed to obtain information at different levels. But transmission electron microscopy (TEM)-related techniques are most suitable for obtaining atomic level information from catalyst particles before, during, and after reaction. This has been recognized for more than 30 years, since the early low-magnification ETEM research on catalysts.[1–4]

In order to observe gas–solid interactions directly, either the TEM column or the sample holder must be modified. In the earliest ETEM studies, different approaches were employed to contain gas (or liquid) environments inside the TEM vacuum column. For *in situ* studies with modest resolution, environmental cell-jigs (ECELLs or microreactors) were designed to be inserted between the objective lens pole pieces of the electron microscope (EM).[1] Typically, pairs of apertures are added on either side of the sample with differential pumping lines attached between them. Reviews of early modifications and the significant scientific impact of ETEM on the chemical and materials sciences are provided by References 4–7. However, these modifications were observed to adversely affect the performance of the TEM, especially the microscope resolution, and necessitated the frequent opening and rebuilding of the microscope. In the late 1980s and 1990s, considerable effort was directed toward incorporating gas cells in the TEM column of medium voltage electron microscopes with better resolution[8,9] based on the design and engineering of Boyes, Doole, and Gai at the University of Oxford. Improved resolution was achieved due to two factors: the availability of medium-voltage TEMs with large objective pole-piece gaps and vibration-free vacuum pumping, based on molecular drag and turbo molecular pumps (MDPs and TMPs, respectively). ETEM and lately E(S)TEM have now been successfully employed to understand the fundamental role of defects in heterogeneous catalysis,[10] bulk diffusion processes in catalysis and electronics,[11] structures in high-temperature superconductors,[12] nanocatalyst sintering,[13] reduction,[14] oxidation,[15] nitridration,[16] polymerization,[17] chemical vapor deposition,[18] electron beam induced deposition,[19,20] hydroxylation,[21] dehydroxylation,[22] and sintering.[23] In this article, we illustrate some recent activities using ETEM, focusing on the development of atomic-resolution ETEM and its applications in the area of gas–solid–liquid reactions for catalysis, polymerization and the fabrication of nanostructured materials such as nanotubes and nanowires, as well as cluster formation during electrochemical deposition at the liquid–solid interface.

The Development of Atomic-Resolution ETEM

The first successful ETEM modification with atomic resolution was of a Philips CM30 developed by Gai and Boyes in 1997.[24,25] This was achieved by extensively modifying the entire EM column of a 300 kV CM30T high-resolution TEM with the introduction of a fully integrated and permanently mounted ECELL system for atomic resolution studies of dynamic gas–solid reactions and *in situ* nanosynthesis. A highlight of this development[25] was the novel ETEM design, with the objective lens pole pieces incorporating radial holes for the first stage of differential pumping (Figure 1). In addition, the regular sample chamber of the ETEM is the controlled environment ECELL. It is separated from the rest of the column by the apertures in each objective pole piece and by the addition of a gate valve in the line to the regular ion-getter pump at the rear of the column. Differential pumping systems are connected between the apertures using MDPs or TMPs. This permits relatively high gas pressures in the sample region, while maintaining high vacuum conditions in the rest of the ETEM column. The design permits detailed tilting of samples for studies of defects which are key to properties of materials, crystallography, chemistry, gas–solid–liquid reactions and the use of regular sample holders.

Dynamic atomic resolution imaging and electron diffraction can be complemented by chemical analysis capability by incorporating Gatan imaging filter-parallel electron energy loss spectroscopy (GIF-PEELS) and a scanning TEM (STEM) attachment.[25–27] A conventional reactor-type gas manifold system enables the introduction of flowing gases into the ETEM, and a sample stage with a furnace (hot stage) permits heating up to 1000°C. For dynamic atomic resolution, a few mbars of gas pressures are routinely used in the ECELL. Higher gas pressures are possible with some loss of resolution due to multiple scattering of electrons through thicker gas layers. A mass spectrometer or residual gas analyzer is added to monitor the composition of gases entering and exiting the sample area. Low electron dose techniques are used for *in situ* experiments to avoid electron beam effects. However, *in situ* data should always be checked in a parallel calibration experiment with the beam off and the sample exposed to the beam only to record the reaction end point. This ensures a completely non-invasive characterization. A video system connected to the ETEM facilitates digitally processed recording of dynamic events in real time, with a time resolution of ~1/30 s.

Under carefully simulated conditions, data from *in situ* ETEM can be related directly to structure–activity relationships in technological processes. Because of the small amounts of solid reactant in the microscope sample, measurement of reaction products is performed on larger samples in a microreactor operating under similar conditions and used for correlation.

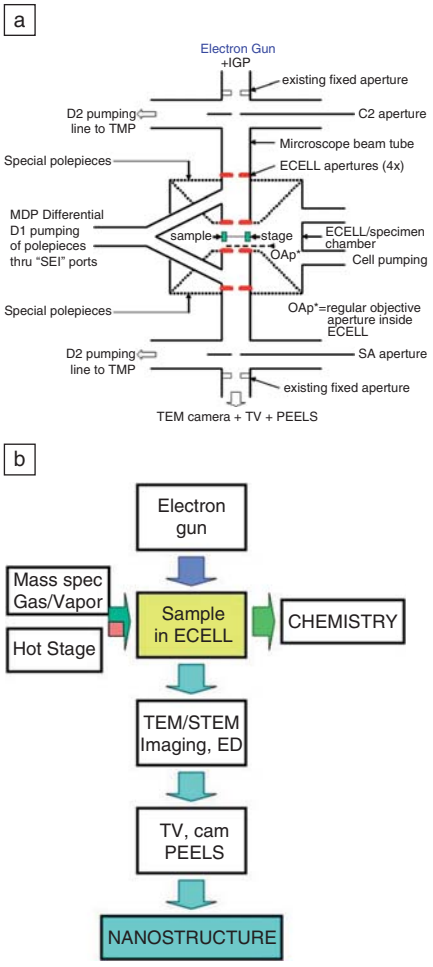

Figure 1. (a) Atomic resolution environmental transmission electron microscopy (ETEM) design of Gai and Boyes:[24,25] schematic representation of the basic geometry of the controlled environment ECELL in a Philips CM30 showing radial holes *through* objective lens pole pieces and the aperture system. The gas inlet, the first stage of differential pumping lines (D1) between the environmental cell apertures, condenser aperture (C2), a second stage of pumping (D2) at the condenser lens, selected area (SA) diffraction aperture, and TEM camera vacuum are indicated. (b) Schematic of the accessories to the ETEM.

The original *in situ* atomic resolution ETEM[24,25] has evolved and later versions have been installed in laboratories throughout the world,[28,29] suggesting that the technique will continue to provide unique information on nanomaterials, as well as catalytic and related processes.

In Situ ETEM in Wet Environments for Polymerization over Nanoparticles on Nanosupports

Many technological hydrogenation and polymerization processes are derived from liquids, and the associated chemical reactions occur on the nanoscale. ETEM can be used to develop novel routes for hydrogenation and polymerization reactions in the liquid phase. For example, novel cobalt promoted-ruthenium nanoparticle catalysts on nanoscale rutile titania support have been developed for the hydrogenation of low vapor pressure aliphatic dinitriles (such as adiponitrile or ADN, $NC(CH_2)_4CN$)), to hexamethylene diamine (HMD, $H_2N(CH_2)_6NH_2$) at temperatures <300°C.[30] HMD is a key intermediate for polymers. Atomic resolution-*in situ* ETEM studies under controlled wet environments at the nanoscale have elucidated novel hydrogenation and polymerization reactions using ADN in the liquid phase and have also revealed a hitherto unknown lattice structure in the resulting organic products. The products can form different compounds under *ex situ* conditions upon exposure to air and CO_2.

A liquid feed heating holder[31,32] shown in Figures 2a and 2b enables *in situ*

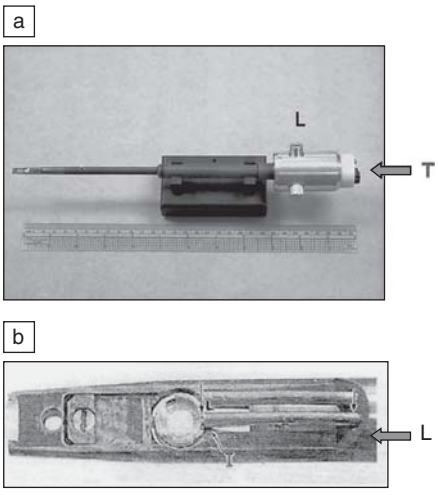

Figure 2. Sample holder for ETEM studies in wet environments: (a) holder with liquid injection tube (L) and heating (T); (b) Enlarged tip of the holder. L and T denote liquid injection tube to the sample in the furnace and the thermocouple, respectively.[31]

nanosynthesis of organic fibers and polymers in liquid–gas–solid environments in the ETEM.[33] Liquid is injected onto the sample via the tube L and gas is inserted using the gas-manifold system of the ETEM. Nanoscale cobalt-promoted Ru on titania nanosupports are highly active, as illustrated in the real-time *in situ* nanosynthesis studies using the ETEM (Figures 3a and 3b). Parallel reactivity studies, performed *ex situ* on larger amounts of the promoted nanocomposite systems, show very high selectivity (Figure 3c), confirming the ETEM findings. During the hydrogenation, partial reduction of nanotitania leads to anion vacancy defects via glide shear mechanism and Ti^{3+}. Electron transfer from the support to Ru reduces Ru *d*-band electron vacancies. In the Co-promoted system, the Co *d*-band vacancies are maintained, which is key to supplying H atoms for the hydrogenation over Ru. The synergistic effect between the nanometals and the interaction with the nanosupport with anion vacancies (associated with Lewis acid sites) provide highly active sites for the reaction.[30] The *in situ* results provide guidelines for designing active sites for hydrogenation processes in general.

In situ wet imaging has simultaneously revealed bis-hexamethylene triamine (BHMT) during the ADN-hydrogenation in the liquid phase. BHMT is used for sealants, coatings and polyamides. Figure 3d shows Co-Ru nanoparticles on nanotitania in ADN liquid at RT, and Figure 3e shows the formation of BHMT fibers at 100°C. Enlargement of the fiber in Figure 3f reveals nanolayers and the lattice structure of BHMT with a periodicity of 0.56 nm. *In situ* polymerization to nylon (6,6) following the reaction of HMD with adipic acid solutions is illustrated by Figures 3g and h: 3g shows the Co-Ru/nanotitania in the solutions at room temperature and Figure 3h shows the formation of the polymer (e.g., at P) at 188°C.

In Situ Atomic Scale Twinning Transformations in Metal Carbides

The dynamical atomic scale reactions in carbides of transition metals, including WC, under reaction conditions are of great importance in fuel cell technologies and nanoelectronics.[34] WC powder systems exhibit extensive atomic scale twin boundary defect structures. WC is hexagonal (space group P-6*m*2), with a = 0.2906 nm and c = 0.2838 nm. The atomic resolution-*in situ* ETEM studies of the same thin area of (100) WC sample in 20% H_2 /He at a pressure of about 3 mbar are shown in Figure 4b. The twins are along [001] with lattice modulations along [010]. Figure 4a shows atomic twin defects at RT and Fig. 4c shows the corresponding electron diffraction (ED). Figures 4b and 4d show the dynamic image and ED, respectively, of the same area at 450°C, reacted for 15 min. Figure 4b demonstrates the elimination of almost all of the twin structures and the transformation to W nano-metal and carbon nanostructures including nanotubes.[34] The presence of the metal was confirmed by the emergence of {100} reflections due to cubic α-W (with a = 0.32 nm) in the parent crystal and by compositional analysis. Similar atomic scale interfacial interactions are important in other transition metal carbides and nitrides.

Measuring Heterogeneity in Complex Oxide Catalysts

Environmental (S)TEM [E(S)TEM] can be employed to relate catalytic properties to the structure and chemistry of individual nanoparticles. For example, the structure and chemistry of active particles can be identified and compared to that of

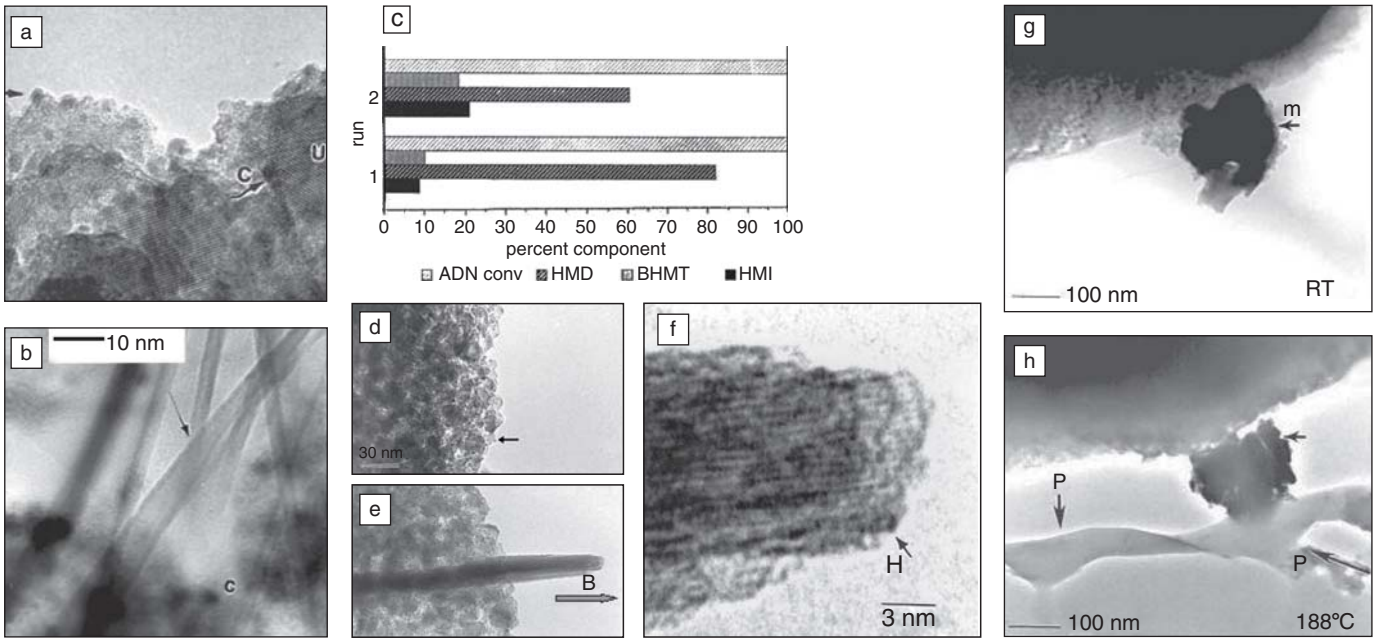

Figure 3. Real time *in situ* liquid–catalyst–gas reactions at the nanoscale in ETEM. (a) Co-Ru nanocatalysts (e.g., at C)/nanotitania (e.g., at U), in vacuum at room temperature (RT). (b) Wet sample: *in situ* hydrogenation of adiponitrile in the liquid phase over the catalyst at ~100°C, showing the desorption of hexamethylene diamine (HMD) nanofibers. The rapid growth of the organic product at ~0.25 nm s^{-1}, indicates a highly selective catalyst. (c) Parallel reactivity tests confirming ETEM data of very high hydrogenation selectivity for Co-Ru nanocatalysts on nanotitania (bar for run number 1) compared to unpromoted Ru catalysts (bar for run number 2). Small amounts of bis-hexamethylene triamine (BHMT) and hexamethylene imine (HMI) are also produced. Full adiponitrile (ADN) conversion is observed.[30] (d) Wet ETEM studies of Co-Ru on nanotitania in ADN liquid and H_2 gas at RT; (e) *In situ* growth of bis-hexamethylene triamine (BHMT) fiber (at H). (f) The enlarged image of the fiber (at H) shows 0.56 nm periodicity of the BHMT lattice. (g) Co-Ru/nanotitania particles (for example, shown at m at the edge of a grid bar used to support sample) in HMD and adipic acid solutions at RT; (h) *In situ* polymerization (e.g., at P) over the catalyst at 188°C.

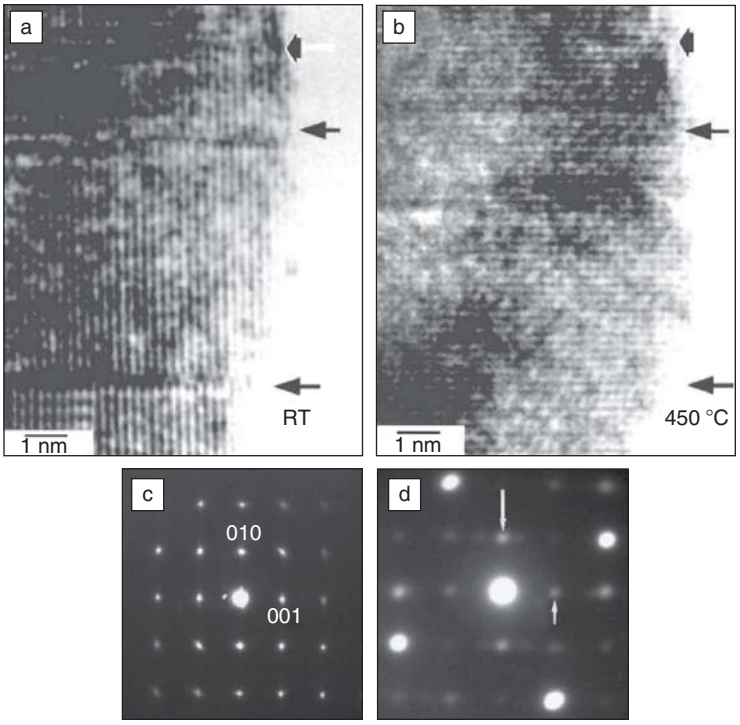

Figure 4. Atomic resolution-*in situ* ETEM studies in real time of dynamic atomic level twinning transformations in (100) tungsten carbide powders in 20% H_2/He at 3 mbar of gas pressure.[34] Images and electron diffraction data are recorded from the same sample area during reactions: (a) atomic scale twin defects at RT (indicated by arrows); (c) electron diffraction at RT; (b) dynamic image at 450°C indicating the elimination of almost all of the atomic twins (arrows); and (d) electron diffraction of (b) at 450°C, indicating the emergence of {100} cubic W reflections (arrowed), and carbon nanostructures in the parent crystal.[34]

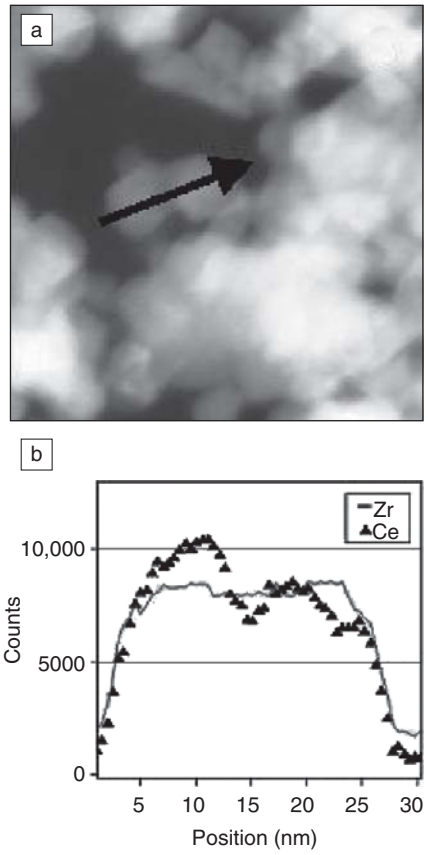

Figure 5. Annular dark-field scanning transmission electron microscopy [(S)TEM] image (a) and electron energy-loss spectroscopy line profile (b) from two individual particles (marked by arrow in the image) in a $Ce_xZr_{1-x}O_2$ solid solution sample. The image and line scans are used to identify CeO_2-rich and ZrO_2-rich solid solution domains at the nanometer scale.

inactive particles. An example of this is shown in Figure 5. The redox temperature of ceria can be lowered by doping with zirconia. Nanoscale characterization of individual particles of a ceria-zirconia sample with nominal composition $CeZrO_2$ reveal both inter- and intra-granular variation in Zr content.[35] Figure 5 demonstrates intergranular heterogeneity across two adjacent particles showing different ceria content. In some cases, chemical heterogeneity is observed within a particle (i.e., with the surface being rich in ceria or vice versa). Interestingly, chemical heterogeneity disappears after the sample is subjected to several redox cycles. Such compositional variations can play an important role in the performance of bimetallic or mixed oxide catalysts.

The Redox Behavior of Ceria-Zirconia Catalysts

The oxidation and reduction behavior of nanoparticles often plays an important role in catalytic processes. Hansen et al.[36] have shown that the morphology and reducibility (the fraction of material reduced) of a Cu/ZnO catalyst changes as a function of the reducing environment. E(S)TEM has also been successfully employed to monitor the redox behavior of individual particles of ceria from the oxidation state of Ce using electron energy loss spectroscopy at different temperatures, as shown by Sharma et al.[36,37] The cerium $M_{4,5}$ ratio (or so called "white-line" ratio) changes as Ce is reduced from the +4 to the +3 state at high temperature in a reducing environment (Figures 6a and 6b). The change in the white-line ratio can be used to monitor the extent of reduction in individual particles with temperature and time (Figure 6c). Such measurements show that the compositional and structural heterogeneity of particles is responsible for the improved reducibility. On the other hand, particles with homogenous composition reduce at lower temperature compared to heterogeneous particles. The ease with which Ce transfers from +4 at high temperature to +3 upon cooling or in an oxidizing environment (the so-called oxygen storage capacity) was lower for particles with higher Ce content. Since doped ceria is also a potential anode material for solid oxide fuel cells, similar measurements will be crucial to identify the optimum composition for the best redox property.

The white-line ratio is also a function of the oxidation state for a number of transition metal oxides such as Fe, Cu, Co, and Mn. Therefore, it is feasible to use the white-line ratio to determine their valence state under reaction conditions.

ETEM Studies of Crystal Growth

We have seen how imaging of nanoparticles in a gaseous environment or under a liquid film can contribute to a detailed understanding of catalyst synthesis and operation. We now discuss the application of ETEM to studies of fundamental crystal growth processes at both the vapor–solid and the liquid–solid interface. TEM has

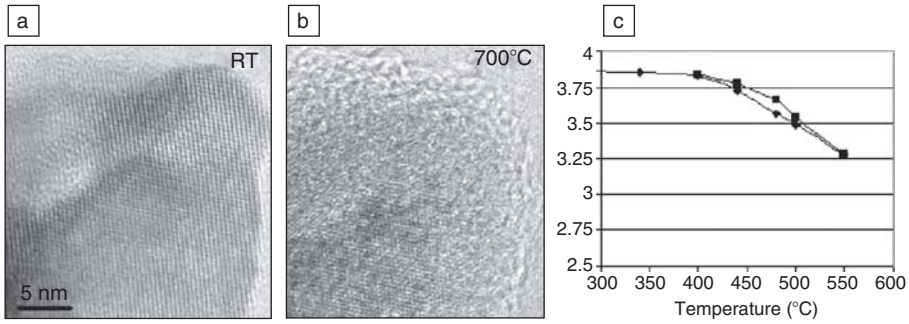

Figure 6. High-resolution images and corresponding background-subtracted Ce $M_{4,5}$ peaks recorded at (a) RT and (b) 700°C in 1.5 Torr of dry H_2 from pure CeO_2 sample showing disordered edges and relative change in the white-line intensity. A small shoulder also disappeared with reduction. (c) Reversibility of the Ce oxidation state for $CeZrO_2$ samples on heating (diamonds) and cooling (squares) in dry H_2. The y-axis is the white-line ratio.

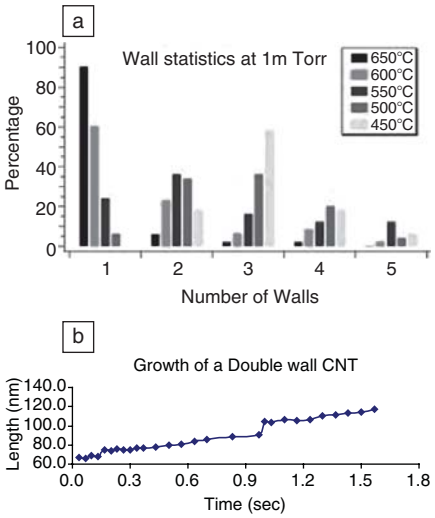

Figure 7. (a) Statistical distribution showing the effect of temperature on the number of walls of CNTs in samples synthesized at different temperatures over time at 1 mTorr of C_2H_2 during *in situ* observation using E(S)TEM. (b) Linear growth rate of a double-walled CNT formed at 550°C using Ni/SiO_2 catalyst in 2.6 mTorr of C_2H_2. Note the irregular growth rate that is related to the formation of a kink.

been widely used for the study of crystal growth (for a recent review see Hawkes and Spence[38]). Quantitative measurements made in a controlled environment can be used to extract the rate-limiting steps during growth, and *in situ* studies can give clues on how to control the nanostructures that form via self-assembly or catalytic processes.

Synthesis of Carbon Nanotubes

In situ observations of the nucleation and growth of one-dimensional nanomaterials have provided an unprecedented insight into and control of their synthesis. One-dimensional nanostructures—nanowires (NWs) and carbon nanotubes (CNTs)—are often synthesized by catalytic chemical vapor deposition. Potential applications require strict control on the diameter, length, and (in the case of CNTs) the number of walls and the chirality: multiwall CNTs with controlled diameter and length are required for field emitters, whereas semiconducting single-walled CNTs are used for transistors. Flowing a carbon-containing precursor such as CH_4, C_2H_2, CO, or alcohol over a transition metal catalyst such as Ni, Fe, Mo, or Co produces a mixture of single-walled and multiwall CNTs, graphene ribbons, and amorphous carbon. Since the sample chamber of an ETEM can be used as a chemical vapor deposition reactor, the formation of these structures can be monitored using time-resolved imaging. The first *in situ* observations of the growth of carbon structures were of filamentous carbon.[2] More recently, high-resolution *in situ* measurements have been used to explain the growth mechanisms and growth conditions of carbon nanofibers and nanotubes.[39–41]

The effect of synthesis conditions (temperature and pressure) on structure was obtained from statistical analysis of data obtained during *in situ* observations of CNT syntheses using ETEM (Figure 7a). In this example, it is interesting to note that although single-walled CNTs are observed to form at temperatures as low as 500°C, their fraction increases continuously with temperature with 95% yield at 650°C in 1 mTorr of C_2H_2.[41] In Figure 7b we show how ETEM can be used to provide information on the kinetics of CNT growth. In order to calculate the number of carbon atoms being used for CNT growth as a fraction of available carbon atoms, the temperature, pressure, number of walls of the nanotube, and its growth rate must be known. Linear growth rates are found from digital videos recorded at synthesis conditions, whereas high-resolution images (or measurements of the inner and outer diameter) show the number of walls in the growing CNT. To calculate the area growth rate, A, it is assumed that the walls of the CNT are perfectly cylindrical and all grow at the same rate and that their radii do not change significantly during growth. We then obtain

$$A = \sum_{n=1}^{N} 2\pi r_n \,.\, E \qquad (1)$$

where r_n is the radius of the nth wall, N is the total number of walls, and E is the average rate of change of length of the nanotube (the linear growth rate). The area of growth is then multiplied by the graphitic areal density of $\sigma = 38.3$ carbon atoms/nm^2 to obtain the number of carbon atoms used per second to grow the nanotube. This type of calculation shows that the number of carbon atoms used to form a CNT is only a fraction of the total flux of carbon atoms provided by the precursor.

These results show some of the exciting possibilities of making atomic level observations of the dynamics of catalyzed nanostructure growth, with new opportunities to understand and monitor atomic level changes during nanoscale synthesis.

Nucleation and Growth of Si and Ge Nanostructures

Because of its importance as a model system and its applications within the semiconductor industry, the epitaxial growth of Si and Ge by chemical vapor deposition has been studied extensively using ETEM. The main difference between such studies and those described in previous sections is the highly reactive nature of the starting materials. This means that an ultrahigh-vacuum (UHV) specimen environment is required so that a clean initial surface can be prepared, usually by annealing at high temperature. UHV electron microscopes are less well suited for higher pressure environmental work of the type described above, and growth is generally observed at lower pressures, up to say 10^{-5} Torr, by leaking the precursor gases directly into the sample area.

One of the most fascinating areas of recent interest is the formation of

semiconductor nanowires. Similarly to CNT formation, nanowires are grown by depositing catalyst particles onto a substrate. The catalyst particles enhance the growth rate locally, resulting in the formation of extended wire-like structures. Unlike CNTs, however, these nanowires can form epitaxially on the substrate under appropriate conditions. Nanowires have applications in electronic devices, information storage, microelectromechanical systems, and perhaps even photovoltaics. For many applications, it is essential to control the structure, orientation, and location of the nanowires, and the factors that determine the growth rate, orientation, and epitaxial relationship with the substrate are therefore of key importance. It is possible to grow wires epitaxially on a substrate that is mounted "vertically" in the TEM, so that the electron beam passes parallel to the substrate surface.[42] The wires then grow perpendicular to the electron beam, allowing growth kinetics to be measured, the catalyst structure to be examined, and the wire surfaces to be characterized during growth.

In Figure 8 we show examples of epitaxial nanowires imaged during *in situ* growth. Figures 8a and 8b show video stills during growth of Si and Ge nanowires via an Au-Si or Au-Ge catalyst, respectively. The liquid nature of the eutectic catalyst droplet is clearly visible from its curved surface and the lack of diffraction contrast. Such videos confirm the "vapor–liquid–solid" model of NW growth,[43] in which incoming flux is collected at the droplet surface and dissolved in the droplet, leading to a supersaturation that drives deposition at the liquid–solid interface. Measurements of growth rates under various conditions allow the rate-limiting steps to be determined, further confirming this model.[44] However, *in situ* studies also demonstrate effects that are not expected from the model, such as surface faceting (Reference 42; Figure 8a) and diffusion of the catalyst during growth.[45] In the case of Ge NWs, *in situ* studies also show an alternative growth mode occurring at temperatures below the bulk eutectic temperature (Figure 8c): vapor–*solid*–solid, where the catalyst is a solid Au particle rather than a liquid Au-Ge eutectic. Unexpectedly, the faster vapor–liquid–solid growth mode also occurs below the eutectic temperature, with the liquid stabilized at low temperatures by the supersaturation of Ge in the droplet.[46]

The vapor–liquid–solid (VLS) growth process in materials such as Si-Au and Ge-Au provides a model system for studying liquid phase epitaxy, particularly the phenomena occurring during nucleation of a solid particle in a supersaturated eutectic liquid. The well-controlled geometry of the wires and droplets means that they can act as mini-reactors accessible to analytical and high-resolution TEM, potentially allowing a variety of interesting observations at the solid–liquid interface. One example is the unexpected kinked morphologies observed when segments of dissimilar materials (such as GaP and Si) are integrated in a single wire.[47]

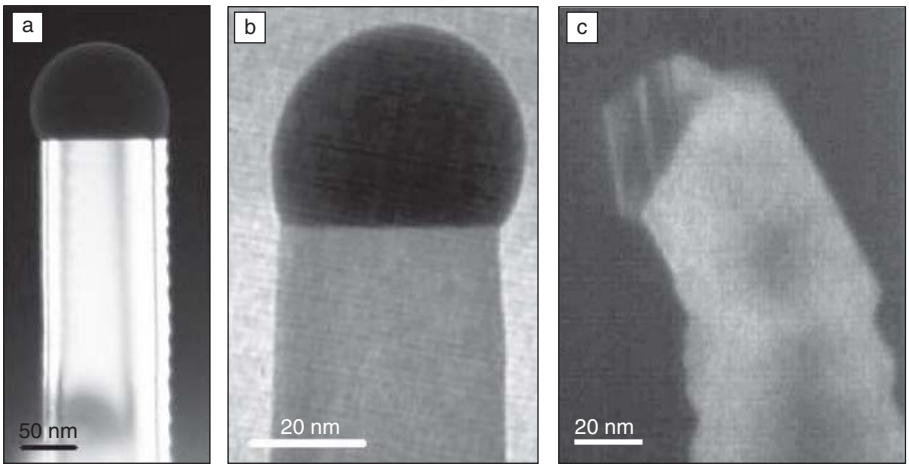

Figure 8. (a) Si nanowire imaged in dark field during growth at 600°C in 2×10^{-6} Torr Si_2H_6. The crystalline wires and the liquid catalyst droplet are clearly visible. Au-induced surface structure consisting of nanoscale facets is visible on the right side (from Reference 42). (b) Ge nanowire imaged in bright field during growth from Ge_2H_6 at 340°C and 4.6×10^{-6} Torr. (c) Ge nanowire imaged in dark field under similar growth conditions, 360°C and 8×10^{-6} Torr, but growing via the vapor–solid–solid (VSS) growth mode. The catalyst is faceted and shows twin contrast characteristic of solid Au.

A quantitative understanding of the important phenomena during NW growth may enable us to design complex structures for advanced applications. However, before this aim can be fully realized, it is necessary to extend UHV ETEM experiments to higher pressures to make the results more relevant to growth in conventional reactors. The techniques described above that have already been pioneered for the study of catalysts will undoubtedly be helpful in achieving this aim.

Electrochemical Deposition at the Liquid–Solid Interface

Electrochemical processes at the liquid–solid interface are important phenomena with applications in energy storage, integrated circuit fabrication, the prevention of corrosion, and the formation of coatings and nanostructured materials. Because electrolytes often have high vapor pressure (in comparison to the eutectic liquids used in vapor-liquid-solid NW growth or the polymers discussed above), the liquid must be fully enclosed to prevent evaporation during the experiment. An additional essential requirement for studying electrochemical processes in the TEM is the need to integrate electrodes. A complete electrochemical cell with three electrodes can provide electrochemical measurements that complement the images that are recorded simultaneously in the TEM. One approach to achieving this[48,49] is shown in Figure 9a, where the liquid is confined between two electron transparent membranes and the electrodes are either patterned into thin films (as shown here for the working electrode) or are composed of wires inserted into the electrolyte (the reference and counter electrodes). In the example shown in Figure 9b, comparison of the current-time transients and the growth kinetics of individual Cu clusters with predictions from electrochemical nucleation and growth models showed that one particular pathway for copper deposition, attachment of Cu onto the surface followed by surface diffusion to an existing cluster, needed to be included to explain the kinetics observed.[49] The effect of the additives that are widely used to change the properties of the deposit, and the spatial correlations between island nucleation sites, can also be examined using *in situ* microscopy.[50,51]

Liquid cells are complex to build but may be adapted for a variety of growth and corrosion processes at the liquid–solid interface, and commercial versions are

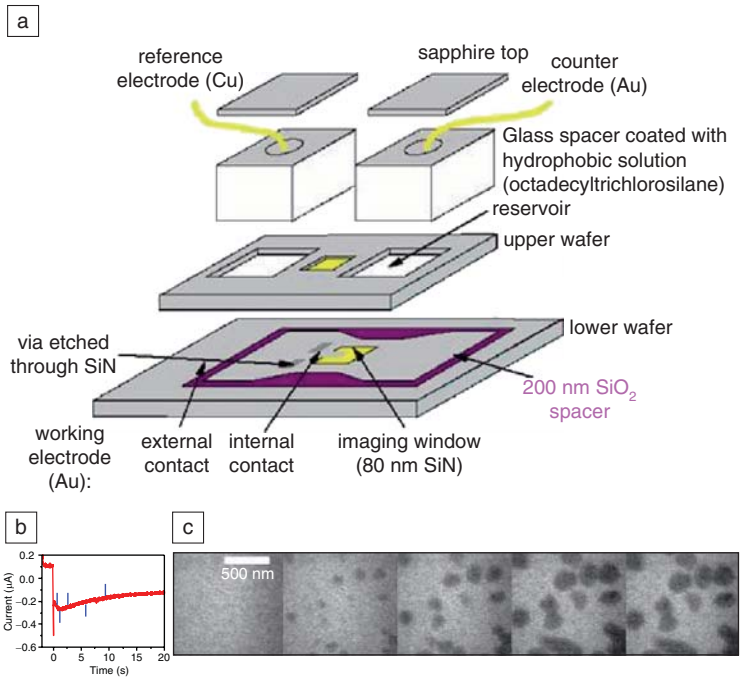

Figure 9. (a) Schematic diagram showing the construction of a liquid cell designed for three-electrode electrochemical experiments in the TEM (adapted from Reference 48). (b) Current-time transient (red curve) and (c) series of bright-field video frames extracted at the times indicated by blue tick marks, showing the nucleation and growth of copper clusters on a polycrystalline Au electrode. The growth was carried out at a constant potential of –0.063V (from Reference 49).

available.[52] Experiments involving water and other high vapor pressure liquids could become easier and hence more widespread if cells such as that in Figure 9a could be combined with microfluidics technology to enable controlled flow, mixing, or heating of liquids.

Conclusions

In this article, we have shown several examples of the application of ETEM for the study of changes in the structure and composition of nanoparticles, the catalytic formation of materials, and growth processes at the gas–solid and liquid–solid interface. It is clear from these and the many other examples in the literature that the ability to impose a controlled environment in the STEM and TEM provides a powerful probe of catalytic, electrochemical, and other reactions. The range of materials and processes studied continues to expand, as the combination of good spatial and temporal resolution with the advanced analytical tools available in modern microscopes provides a unique window into nanoscale processes. Despite the experimental complexity, ETEM studies are essential for improving our understanding of nanostructure formation, catalysis, and other nanoscale processes that have both industrial and academic importance.

Acknowledgments

P.L.G. thanks E.D. Boyes and L.G. Hanna (DuPont) for collaborations on E(S)TEM column design and development and R.C. Doole for earlier collaborations at Oxford. R.S. thanks P. Crozier and K. Weiss (Arizona State University) for E(S)TEM modifications, the use of the John Cowley Center for High Resolution Electron Microscopy, and funding from the National Science Foundation and the U.S. Department of Energy. F.R. thanks R.M. Tromp, M.C. Reuter, and A. Ellis for their development of the UHV TEM, and the National Science Foundation and Defense Advanced Research Projects Agency for their financial support.

References

1. P.R. Swann, N.J. Tighe, *Jern. Ann.* **155**, 251 (1971).
2. R.T. Baker, P.S. Harris, R.B. Thomas, R.J. Waite, *J. Catal.* **30**, 86 (1973).
3. P.L. Gai, W. Thoni, P.B. Hirsch, *Philos. Mag.* **35**, 781 (1979).
4. E.P. Butler, K.F. Hale, *Dynamic Experiments* (North Holland, Amsterdam, 1981).
5. P.L. Gai (-Boyes), *Catal. Rev. Sci. Eng.* **34**, 1 (1992).
6. I.M. Robertson, D. Teter, *Microsc. Res. Tech.* **42**, 260 (1998).
7. R. Sharma, *Microsc. Microan.* **7**, 494 (2001).
8. G.M. Parkinson, *Catal. Lett.* **2**, 303 (1989).
9. R.C. Doole, G.M. Parkinson, J.M. Stead, *Inst. Phys. Conf. Ser.* **119**, 157 (1991).
10. P.L. Gai, *Philos. Mag.* **43**, 841 (1981); and *J. Solid State Chem.* **49**, 25 (1983).
11. P.L. Gai, B.C. Smith, *Nature* **348**, 430 (1990).
12. P.L. Gai, E.M. McCarron, *Science* **247**, 553 (1990).
13. P.L. Gai, B.C. Smith, *Ultramicroscopy* **34**, 17 (1990).
14. P.A. Crozier, R. Sharma, A.K. Datye, *Microsc. Microan.* **4**, 278 (1998).
15. M.J. Sayagués, J.L. Hutchison, *J. Solid State Chem.* **143**, 33 (1999).
16. R. Sharma, E. Schweda, D. Naedele, *Chem. Mater.* **13**, 4014 (2001).
17. V.P. Oleshko, P.A. Crozier, R.D. Cantrell, A.D. Westwood, *J. Electron. Microsc.* **51**, S27 (2002) (Suppl.).
18. J. Drucker, R. Sharma, J. Kouvetakis, J.K. Weiss, *J. Appl. Phys.* **77**, 2846 (1995).
19. P.A. Crozier, J. Tolle, J. Kouvetakis, C. Ritter, *Appl. Phys. Lett.* **84**, 3441 (2004).
20. W. van Dorp, R. van Someren, C. Hagen, P. Kruit, P.A. Crozier, *Nano Lett.* **5**, 1303 (2005).
21. R. Sharma, M.J. McKelvy, H. Béarat, A.V.G. Chizmeshya, R.W. Carpenter, *Philos. Mag.* **84**, 2711 (2004).
22. M.J. McKelvy, R. Sharma, AV.G. Chizmeshya, R.W. Carpenter, K. Streib, *Chem. Mater.* **13**, 921 (2001).
23. R.-J. Liu, P.A. Crozier, C.M. Smith, D. Hucul, J. Blackson, G. Salaita, *Appl. Catal. A* **282**, 111 (2005).
24. P.L. Gai, K. Kourtakis, et al., *Science* **267**, 661 (1995).
25. E.D. Boyes, P.L. Gai, *Ultramicroscopy* **67**, 219 (1997).
26. R. Sharma, P.A. Crozier, *Transmission Electron Microscopy for Nanotechnology,* Z.L. Wang, Ed., 531 (Springer-Verlag and Tsinghua University Press, 2005).
27. C. Lopez-Cartes, S. Bernal, J.J. Calvino, M. Cauqui, G. Blanco, J. Perez-Omil, J. Pintado, S. Helveg, P.L. Hansen, *Chem. Comm.* 644 (2003).
28. J. Haggin, *Am. Chem. Soc. Chem. Eng. News* **73** (30), 39 (1995).
29. M. Jacoby, *Am. Chem. Soc. Chem. Eng. News* **80** (31), 26 (2002).
30. P.L. Gai, K. Kourtakis, E.D. Boyes, *Catal. Lett.* **102**, 1 (2005).
31. P.L. Gai, *Microsc. Microan.* **8**, 21 (2002).
32. P.L. Gai, E.D. Boyes, *Electron Microscopy in Heterogeneous Catalysis* (Institute of Physics Publ., UK, USA, 2003).
33. J.M. Thomas, P.L. Gai, *Adv. Catal.* **48**, 171 (2004).
34. P.L. Gai, C.C. Torardi, E.D. Boyes, Ch. **45**, 745: *Turning Points in Soid State Chemistry*, (Eds: K.D.M. Harris and P.P.Edwards), Royal Society of Chemistry U.K. (2007).
35. R. Wang, P.A. Crozier, R. Sharma, J. Adams, *J. Phys. Chem. B* **110**, 18278 (2006).
36. T.W. Hansen, J. Wagner, P.L. Hansen, S. Dahl, H. Topsoe, J. Jacobsen, *Science* **294**, 1504 (2001).
37. R. Sharma, P.A. Crozier, Z.C. Kang, L. Eyring, *Philos. Mag.* **84**, 2731 (2004).
38. P.W. Hawkes, J.C. Spence, Eds., *Science of Microscopy* (Springer, 2006).
39. S. Helveg, C. Lopez-Cartes, J. Sehested, P.L. Hansen, B. Clausen, J. Rostrup-Nielsen, F. Abild-Pedersen, J. Norskov, *Nature* **427**, 426 (2004).

40. S.R. Hofmann, R. Sharma, C. Ducati, G. Du, C. Mattevi, C. Cepek, M. Cantoro, S. Pisana, A. Parvez, F. Cervantes-Sodi, A.C. Ferrari, R. Dunin-Borkowski, S. Lizzit, L. Petaccia, A. Goldoni, J. Robertson, *Nano Lett*. **7**, 602 (2007).
41. R. Sharma, P. Rez, M. Brown, G.H. Du, M.M.J. Treacy, *Nanotechnology* **18**, 125602 (2007).
42. F.M. Ross, J. Tersoff, M.C. Reuter, *Phys. Rev. Lett*. **95**, 146104 (2005).
43. R.S. Wagner, W.C. Ellis, *Appl. Phys. Lett*. **4**, 89 (1964).
44. S. Kodambaka, J. Tersoff, M.C. Reuter, F.M. Ross, *Phys. Rev. Lett*. **96**, 096105 (2006).
45. J.B. Hannon, S. Kodambaka, F.M. Ross, R.M. Tromp, *Nature* **440**, 45 (2006).
46. S. Kodambaka, J. Tersoff, M.C. Reuter, F.M. Ross, *Science* **316**, 729 (2007).
47. K.A. Dick, S. Kodambaka, M.C. Reuter, K. Deppert, L. Samuelson, W. Seifert, L.R. Wallenberg, F.M. Ross, *Nano Lett*. **7**, 1817 (2007).
48. M.J. Williamson, R.M. Tromp, P.M. Vereecken, R. Hull, F.M. Ross, *Nat. Mater*. **2**, 532 (2003).
49. A. Radisic, P.M. Vereecken, J.B. Hannon, P.C. Searson, F.M. Ross, *Nano Lett*. **6**, 238 (2006).
50. A. Radisic, P.M. Vereecken, P.C. Searson, F.M. Ross, *Surf. Sci*. **600**, 1817 (2006).
51. A. Radisic, F.M. Ross, P.C. Searson, *J. Phys. Chem. B* **110**, 7862 (2006).
52. http://www.hummingbirdscientific.com/products/liquid_cell_holder/product_FH_2000_TEM.pdf. □